

Semantic-Contact Fields for Category-Level Generalizable Tactile Tool Manipulation

Kevin Yuchen Ma^{1,2}, Heng Zhang^{1,3}, Weisi Lin³, Mike Zheng Shou² and Yan Wu¹

¹Robotics & Autonomous Systems Division, Institute for Infocomm Research, Agency for Science, Technology and Research (A*STAR-I²R), Singapore
wuy@i2r.a-star.edu.sg

²Show Lab, National University of Singapore, Singapore
yuchen_ma@u.nus.edu, mikeshou@nus.edu.sg

³College of Computing and Data Science, Nanyang Technological University, Singapore
HENG018@e.ntu.edu.sg, wslin@ntu.edu.sg

Project Website: <https://kevinskwk.github.io/SCFields>

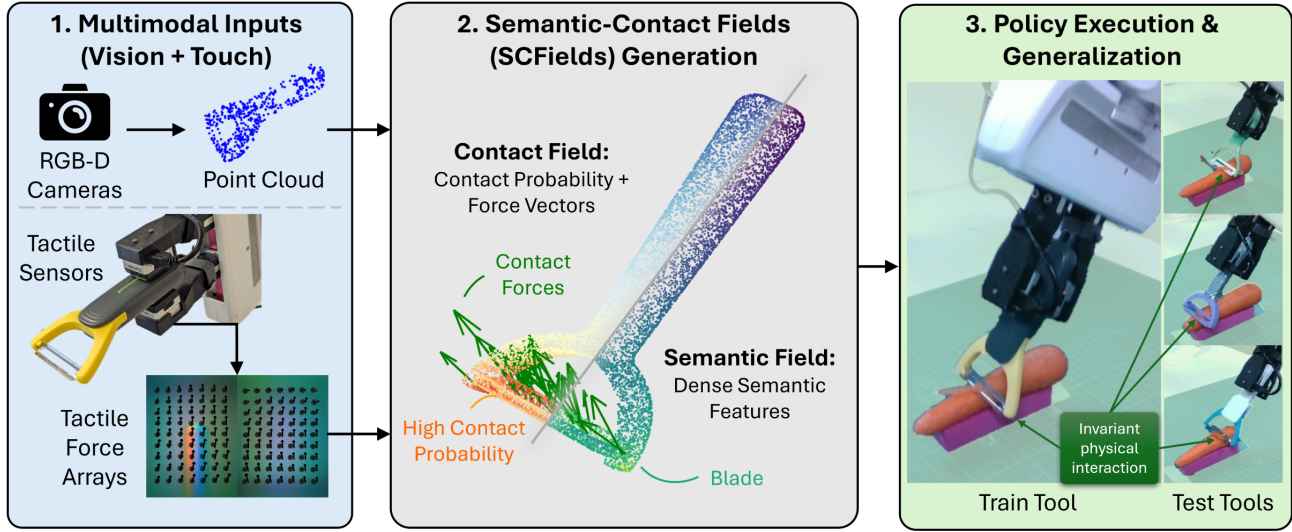


Fig. 1: **Semantic-Contact Fields (SCFields) Overview.** **1. Multimodal Inputs:** The system takes RGB-D observations and tactile readings from GelSight sensors. **2. SCFields Generation:** Our unified perception module fuses these inputs into a dense point cloud representation containing both category-level semantics (blue/green heatmap) and extrinsic contact force vectors (green arrows). **3. Policy Execution:** A diffusion policy conditioned on the SCFields enables zero-shot generalization to novel tools variants (e.g., peelers of different shapes) in contact-rich tasks by reasoning about functional affordance and contact forces simultaneously.

Abstract—Generalizing tool manipulation requires both semantic planning and precise physical control. Modern generalist robot policies, such as Vision-Language-Action (VLA) models, often lack the high-fidelity physical grounding required for contact-rich tool manipulation. Conversely, existing contact-aware policies that leverage tactile or haptic sensing are typically instance-specific and fail to generalize across diverse tool geometries. Bridging this gap requires learning unified contact representations from diverse data, yet a fundamental barrier remains: diverse real-world tactile data are prohibitive at scale, while direct zero-shot sim-to-real transfer is challenging due to the complex dynamics of nonlinear deformation of soft sensors.

To address this, we propose Semantic-Contact Fields (SCFields), a unified 3D representation fusing visual semantics with dense contact estimates. We enable this via a two-stage Sim-to-Real Contact Learning Pipeline: first, we pre-train on a large

simulation data set to learn general contact physics; second, we fine-tune on a small set of real data, pseudo-labeled via geometric heuristics and force optimization, to align sensor characteristics. This allows physical generalization to unseen tools. We leverage SCFields as the dense observation input for a diffusion policy to enable robust execution of contact-rich tool manipulation tasks. Experiments on scraping, crayon drawing, and peeling demonstrate robust category-level generalization, significantly outperforming vision-only and raw-tactile baselines.

I. INTRODUCTION

Tool use represents a hallmark of intelligence, extending a robot’s physical capabilities beyond its own embodiment. However, achieving robust category-level generalization in tool manipulation remains challenging. Effectively manipulating

diverse tool variants requires a dual understanding: a semantic grasp of *where* to hold and apply the tool (functional affordance) and a physical mastery of *how* to regulate interaction forces (contact dynamics).

While recent advances in large-scale robotic learning have produced generalist policies capable of interpreting high-level semantic commands, these vision-centric models remain physically naive. Methods relying solely on 3D visual representations, such as GenDP [29], can generalize geometrically across tool variants, but fail in contact-rich tasks that are visually ambiguous and require precise force regulation. Conversely, policies that leverage tactile or haptic sensing [2, 18] are adept at managing local contact, but are typically instance-specific. Because they map tactile signals directly to actions without an intermediate generalized representation, they fail to adapt when the tool’s geometry changes.

Our approach is grounded in a key physical insight: while the global geometry of tools within a category varies significantly, the physical interaction at the “effective part”—such as the blade of a peeler—remains invariant. Therefore, an explicit representation of this extrinsic contact allows a policy to transfer manipulation skills across diverse tool geometries. A promising candidate for this is the contact field [7], which maps tactile feedback onto the tool’s surface. However, learning this representation presents a dilemma: collecting diverse real-world tactile data to cover all geometries is prohibitively expensive, yet training entirely in simulation introduces a severe Sim-to-Real gap. Simulating the non-linear deformation of soft tactile sensors is notoriously difficult, leading models trained solely in simulation to hallucinate phantom forces or miss contacts entirely when deployed.

To bridge this gap, we propose the **Semantic-Contact Fields (SCFields)** (Figure 1), a unified 3D representation trained via a holistic Sim-to-Real framework. We decompose the contact estimation problem into learning *general geometry and interaction physics* (invariant contact distributions) and *real-world sensory alignment* (sensor-specific signal interpretation). Accordingly, our pipeline operates in two distinct stages. First, we leverage large-scale simulation to train our model on a diverse dataset of tools, establishing strong physical priors for the invariant contact physics. Second, to address the reality gap, we introduce a **Real-World Alignment** stage. We generate pseudo-labels using geometric heuristics and analytical methods from a small set of simple real-world interactions. This alignment step adapts the simulation-trained model to interpret real sensor responses while preserving the generalizable physics learned in simulation. Importantly, the data used for this alignment stage is collected concurrently with the demonstrations used for imitation learning policy training, meaning no additional, separate data collection effort is required.

Our specific contributions are as follows:

- We propose the **Semantic-Contact Fields (SCFields)**, an invariant 3D representation that fuses semantic features from pre-trained vision models with dense, extrinsic contact estimates.

- We introduce a comprehensive **Sim-to-Real training pipeline** that combines the scalability of simulation with the fidelity of real-world data. By pre-training on diverse simulated tools and fine-tuning with heuristic-labeled real data, we achieve robust dense contact estimates generalizable to unseen tool variants.
- We evaluate our approach on a Franka Panda robot with Gelsight Mini tactile sensors across three distinct tasks: scraping, crayon drawing, and peeling. We demonstrate that our pipeline enables generalization to unseen tool instances and robustness to environmental variations.

II. RELATED WORK

A. Generalizable 3D Manipulation and Tool Use

A key limitation of 2D image-based policies is their sensitivity to viewpoint changes. This has led to a surge in 3D-centric policies that operate directly on point clouds or neural fields [32, 5, 11, 34], providing improved spatial reasoning. To enable category-level generalization, recent works have adopted semantic-centric representations. Methods like D3Field [28] and GenDP [29] utilize 3D semantic fields—dense per-point features that capture functional understanding—to condition diffusion policies. While these methods achieve remarkable geometric generalization, they remain purely vision-based and physically naive, struggling in contact-rich tasks where visual semantics alone are insufficient.

In the domain of tool manipulation, generalization requires understanding both geometry and function. Prior works address this by learning structured correspondences between tool instances. Some approaches focus on dense alignment, predicting motion fields or 6D functional poses to map dynamics across tools [22, 30]. Other methods utilize sparser representations to enable one-shot skill transfer, modeling tools via functional keypoints [25, 26] or leveraging vision-language models to identify affordance regions [24, 16]. While successful at identifying *where* the functional part of a tool is (geometric generalization), these methods often overlook the *contact dynamics* required to execute the task (physical generalization), such as the precise force required to peel or scrape.

Attempts to bridge this gap by combining vision and touch have yielded promising but limited results. 3D-ViTac [10] integrates tactile readings as occupancy points into a scene point cloud, but this primarily captures static geometry rather than dynamic forces. Other works rely on wrist force-torque sensors for compliance [18, 6, 17]. However, for tool manipulation, wrist-mounted sensing is often insufficient, as critical interaction forces at the tool tip are masked by the tool’s own leverage and dynamics. Our work addresses this by proposing a unified representation that is both tool-invariant (like semantic fields) and force-aware at the point of contact.

B. Tactile Perception and Sim-to-Real Transfer

The primary challenge in leveraging the tactile modality is converting high-dimensional, noisy sensor data into a useful representation. Vision-based sensors like GelSight [31]

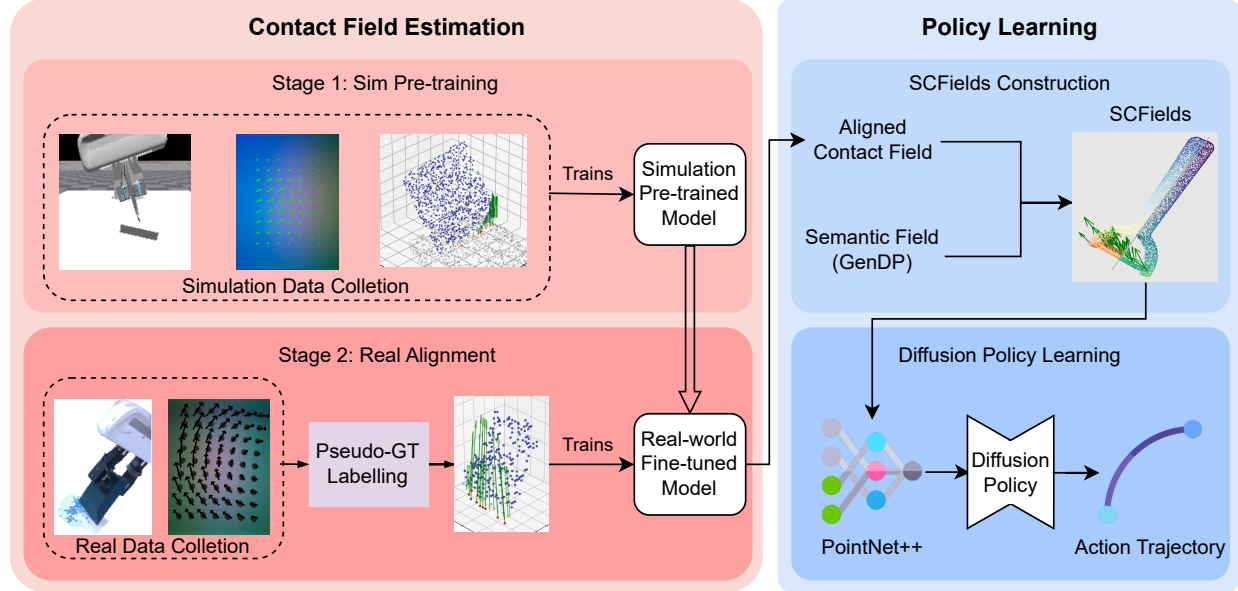


Fig. 2: **Method Overview.** **Left:** Contact Field Learning (III-B) Stage 1 learns the general geometry and contact physics in simulated data; Stage 2 aligns sensor domain with pseudo-labeled real data. **Right:** Policy Learning (III-C) A Diffusion Policy is trained conditioned on the combined SCFields to achieve robust tool manipulation.

provide rich, high-resolution topography, while taxel-based sensors offer direct force maps. Recent advances in tactile representation learning, such as T3 [33] and Sparsh [9], utilize self-supervision to learn robust encoders. However, these representations typically focus on intrinsic tactile features (direct sensor readings) rather than explicit spatial grounding (where the contact is on the tool), limiting their utility for precise tool dynamics modeling.

Tactile manipulation is further hindered by the significant gap between simulated and real tactile physics. General tactile simulators [27, 23, 1] have made strides in modeling sensor deformation and optical properties. However, accurately capturing fine-grained contact mechanics—such as friction coefficients, hysteresis, and soft-body dynamics—remains computationally intensive and difficult to calibrate. As a result, policies trained purely in simulation [3, 15, 1] often struggle to generalize to the unmodeled physical variations of the real world. To address this, we propose a real-world alignment strategy: by finetuning our contact estimator on a small set of heuristically labeled real-world data, we bridge the sensory gap efficiently without requiring high-fidelity simulation.

C. Extrinsic Contact Estimation

To manipulate tools effectively, a robot must understand *extrinsic contact*—the interaction between the tool and the environment. Prior work has attempted to estimate this property through various means. Vision-only approaches [12] are ungrounded and ambiguous without actual tactile feedback, while analytical methods [19] often rely on known object geometries and specific exploratory motions.

The most promising recent direction involves learning implicit contact representations. Neural Contact Fields (NCF) [7, 8] learn a continuous function mapping surface coordinates to contact probabilities. However, NCF assumes a fixed in-

hand pose of the tool relative to the sensor, which breaks down during dynamic manipulation where grasp adaptation occurs. More recent work like VitaScope [13] relaxes this assumption by jointly estimating the tool in-hand pose and the extrinsic contact. However, VitaScope requires a known tool mesh, preventing generalization to unseen tools. Furthermore, these methods typically model contact probability via geometric proximity, ignoring the magnitude of contact forces. In contrast, our Semantic-Contact Fields handle varying tool poses via a point-cloud-centric architecture and explicitly estimate contact forces alongside contact probability, enabling robust manipulation of novel tools.

III. METHODS

Our goal is to learn a manipulation policy that generalizes to unseen tool variants by leveraging contact-rich dynamics. To achieve this, we propose a two-stage method (Figure 2):

- 1) **Contact Field Learning:** We train a multimodal perception model f_ϕ to estimate a dense Extrinsic Contact Field on the tool surface. This model is pre-trained in simulation to learn physical priors and fine-tuned on real-world data for domain alignment.
- 2) **Policy Learning:** We construct a unified state representation by fusing these estimated contact probabilities and forces with 3D Semantic Fields [29]. This fused representation conditions a diffusion policy π_θ capable of zero-shot transfer to novel tool instances.

A. Problem Formulation

We formulate the system as two distinct learning problems:

1. **Extrinsic Contact Field Estimation:** We learn a perception mapping f_ϕ that transforms raw observations—tool and environment point clouds ($P_{\text{tool}}, P_{\text{env}}$), tactile sensor readings

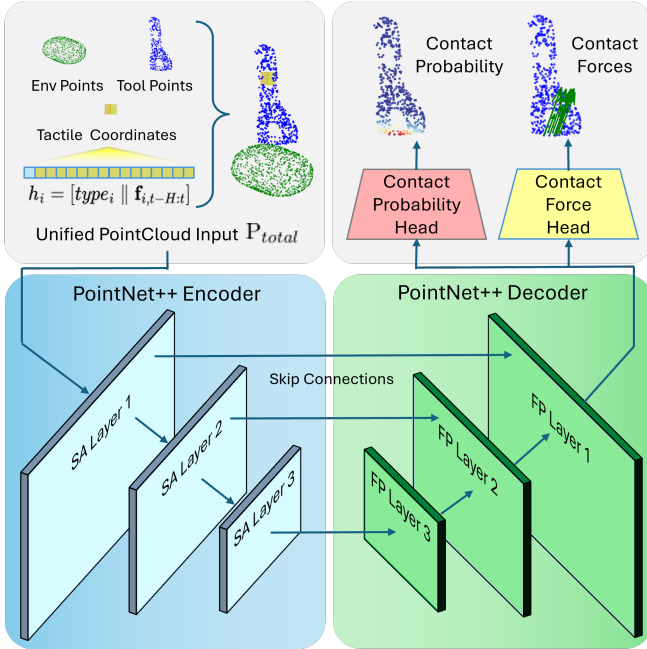


Fig. 3: Contact field model architecture. The network fuses tactile markers and force arrays with dense object geometry in a unified point cloud input to predict contact fields.

(T), and proprioceptive state (q)—into a dense extrinsic contact field F_c over the tool surface. This field assigns a contact probability c_i and a 3D force vector f_i to every point p_i in the tool point cloud P_{tool} .

2. Generalizable Policy Learning: We treat manipulation as conditional generation. We learn a policy $\pi_\theta(a_{t:t+H}|O_t)$ that predicts a sequence of actions a given observation O_t . The core challenge is designing an O_t that is invariant to instance-specific geometry while retaining high-fidelity physical feedback.

B. Contact Field Estimation

1) Model Architecture: Unlike prior works that process vision and touch with separate encoders [7], we employ a unified **Tactile-as-PointCloud** architecture similar to 3D-ViTac [10]. We treat tactile signals as 3D geometric entities, fusing them directly into the scene geometry using a PointNet++ [21] framework (Figure 3).

Unified Input Representation. The input is a composite point cloud $P_{\text{total}} = P_{\text{obj}} \cup P_{\text{env}} \cup P_{\text{tactile}}$, where P_{obj} and P_{env} represent the sampled tool and environment surfaces, and P_{tactile} represents the 3D coordinates of the tactile sensor markers projected into the world frame.

Each point $p_i \in P_{\text{total}}$ is augmented with a feature vector $h_i = [\text{type}_i \parallel \mathbf{f}_{i,t-H:t}]$. Here, type_i encodes the source (Object, Env, Tactile), and $\mathbf{f}_{i,t-H:t}$ encodes a H -step history of marker displacements. This representation allows the network to implicitly learn the relationship between tool geometry, sensor deformation, and contact location without a dedicated pose encoder.

Network Architecture. We process P_{total} using a standard

PointNet++ encoder-decoder. The encoder fuses sparse tactile signals with dense tool geometry based on spatial proximity. The decoder upsamples the features back to the resolution of P_{obj} , effectively propagating localized sensor information to the entire tool surface. Two parallel heads then predict the scalar contact probability $c_i \in [0, 1]$ and regress the extrinsic force vector $\mathbf{f}_i^{\text{ext}} \in \mathbb{R}^3$ for each point. Detailed layer configurations are provided in Appendix A.

2) Simulation Data Generation: Training requires dense ground-truth (GT) labels for contact locations and forces, which are physically inaccessible in the real world. We address this by generating a large-scale synthetic dataset (300 tool instances, 320,000 frames) using a multi-simulator pipeline, inspired by [13].

Simulation Pipeline. We construct a simulation environment comprising a Franka Emika Panda robot and diverse procedurally generated tools (scrapers, crayons, peelers). Data collection proceeds in two steps:

- 1) Interaction (IsaacGym + TacSL):** We use IsaacGym [20] for high-throughput rigid-body dynamics and TacSL [1] to simulate the specific force field and depth data of GelSight sensors.
- 2) Labeling (Open3D + PyBullet):** Since accurate contact locations and forces are not directly accessible in IsaacGym, we employ a replay strategy. We replicate the scene in Open3D to compute signed distance functions (SDF) for soft contact probability, and replay interactions in PyBullet to extract discrete contact forces, which are then extrapolated to the dense point cloud.

This pipeline produces dense, physically consistent labels for 300 unique tool geometries. Further details on the replay and extrapolation logic are in Appendix B.

3) Real-World Pseudo-GT Generation: Despite efforts of filtering and calibration, significant gap still exists between the simulated tactile force field and the marker displacement on real sensors. Furthermore, obtaining dense ground-truth extrinsic contact fields directly in the real world is extremely difficult, as it would require instrumenting the entire surface of arbitrary tools with high-resolution force sensors. To bridge these challenges, we introduce a **Real-World Alignment** stage. We collect a small calibration dataset of real-world interactions and generate "Pseudo-Ground Truth" labels using geometric heuristics and analytical force optimization.

Heuristic Contact Probability. We constrain data collection to a structured task: scraping a flat surface with known table height z_{table} . We first identify geometrically plausible contact candidates $C_{\text{candidate}} \subset P_{\text{obj}}$ using a height threshold ($p_z < z_{\text{table}} + \epsilon$). To eliminate false positives (e.g., the tool hovering near the surface without touching), we apply a signal-based gating filter. We compute the mean magnitude of tactile marker displacements relative to the initial undeformed frame. A frame is labeled as "in contact" only if this mean delta signal exceeds a calibrated noise threshold. For these valid frames, points in $C_{\text{candidate}}$ are assigned soft contact probability labels $c_i \in [0, 1]$ inversely proportional to their distance from the

table surface.

Analytical Contact Force Optimization. To estimate dense force vectors \mathbf{f}_i^{ext} without ground-truth from external force sensors, we solve a convex optimization problem that explains the observed tactile net wrench \mathbf{W}_{tac} using a distribution of point forces \mathbf{f} at candidate contact points. We formulate this as a Second-Order Cone Program (SOCP):

$$\min_{\mathbf{f}} \quad \|\mathbf{G}\mathbf{f} - \mathbf{W}_{tac}\|_2^2 + \lambda \sum_{i \in C_{candidate}} \frac{\|\mathbf{f}_i\|_2^2}{c_i + \epsilon} \quad (1)$$

$$\text{s.t.} \quad \|\mathbf{f}_i\|_2 \leq 2(\mathbf{f}_i \cdot \mathbf{n}_i) \quad \forall i \quad (2)$$

where \mathbf{G} is the grasp matrix mapping point forces to the gripper frame. The objective minimizes wrench discrepancy while regularizing force magnitudes inversely to their heuristic contact probability c_i , favoring geometrically likely contact points. The constraint enforces physical plausibility by bounding force magnitude by twice its projection onto the inward normal \mathbf{n}_i . This ensures forces are compressive and lie within a $\sim 60^\circ$ friction cone, preventing unrealistic "pulling" or shear. The problem is solved efficiently using the ECOS solver [4].

4) *Two-Stage Model Training:* We employ a two-stage strategy to transfer physical priors from simulation to the real world. Both stages minimize a composite loss $\mathcal{L}_{total} = \lambda_{prob}\mathcal{L}_{prob} + \lambda_{force}\mathcal{L}_{force}$. We use Focal Loss [14] for \mathcal{L}_{prob} to handle class imbalance, and a combination of Adaptive Weighted MSE (magnitude) and Cosine Similarity (direction) for \mathcal{L}_{force} . Detailed training and loss function hyperparameters are presented in Appendix C.

Stage 1: Sim Pre-training. The model is first trained on the large-scale simulation dataset with extensive domain randomization. This establishes the fundamental mapping between tool geometry and force distribution across a wide range of tool variants and interaction poses.

Stage 2: Real-World Alignment. We fine-tune the model on the pseudo-labeled real-world dataset. Since this real-world set is small and collected under constrained conditions, we apply random translation and rotation augmentations to the input point clouds during training to enhance data diversity, preventing overfitting to the specific collection poses and ensuring that the learned sensor alignment generalizes robustly to varied spatial configurations. We use a reduced learning rate to adapt to the real sensor characteristics while preserving the general physical priors learned in simulation.

C. Semantic-Contact Fields for Policy Learning

To bridge the definition gap identified in Section III-A, we construct the **Semantic-Contact Fields (SCFields)**—a unified 3D observation fusing semantics and contact physics. The policy observation s_t is a dense feature field over the object point cloud P_{obj} . Each point p_i carries a feature vector $x_i = [\mathbf{f}_i^{ext} \parallel c_i \parallel S_i]$, where:

- \mathbf{f}_i^{ext}, c_i : The **Aligned Contact Field** estimates (force and probability) from our fine-tuned contact estimation module.
- S_i : **3D Semantic Fields** adapted from [29] extracted from a pre-trained vision backbone. These capture functional

semantics (e.g., "blade" vs "handle"), providing geometric invariance.

We implement the manipulation policy π_θ using a 3D Diffusion Policy framework based on [29]. The dense SCFields point cloud $\{p_i, x_i\}$ is first processed by a PointNet++ backbone to extract a global feature vector that aggregates both semantic and physical information. This feature vector is then fed into the diffusion policy's denoising network as the conditioning input. During inference, the policy iteratively denoises random Gaussian noise into a sequence of end-effector actions $a_{t:t+H}$, guided by the geometry-aware features extracted from the SCFields.

IV. EXPERIMENTS

We design our experiments to evaluate two main hypotheses: (1) Does our unified *Tactile-as-PointCloud* architecture, combined with real-world alignment, produce accurate contact estimates that generalize to unseen tools? (2) Does the resulting **Semantic-Contact Fields (SCFields)** enable a diffusion policy to perform contact-rich manipulation tasks that are robust to environmental variations and novel tool instances?

A. Contact Field Model Evaluation

We first validate the contact field perception module (f_ϕ) in isolation to ensure it provides reliable contact probability and force vector estimates before integrating it into the policy loop.

Models Compared. To isolate the contributions of our architecture and training pipeline, we categorize comparisons as follows:

1. *Sim-to-Real Training Strategies (Validating the Pipeline):*
 - **Ours (Aligned):** Pre-trained on large-scale simulation, then fine-tuned on the small real-world scraper dataset.
 - **Sim-Only:** Trained exclusively on simulation data. Evaluates zero-shot transfer and the magnitude of the sim-to-real gap.
 - **Real-Only:** Trained from scratch on the small real-world scraper dataset. Tests if physical priors from simulation are necessary given limited real data.
2. *Baselines & Ablations (Validating the Architecture):*
 - **No-Tactile:** Identical architecture with tactile marker features masked out. This baseline forces the model to rely solely on geometric intersection (P_{obj} vs P_{env}), testing the necessity of dynamic tactile feedback.
 - **NCF (Neural Contact Fields) [7]:** A baseline implicit representation that predicts contact probabilities but lacks explicit force vector regression.
 - **Ablation - 2D Tactile Encoder:** Replaces our point-cloud fusion with a standard CNN encoder for the tactile force arrays, concatenated with the global point cloud feature. This tests the benefit of our *Tactile-as-PointCloud* fusion strategy.
 - **Ablation - Loss Function:** Replaces Focal Loss with standard BCE Loss to evaluate robustness to class imbalance.

TABLE I: Sim Evaluation: Architecture Capacity

Model	F1 Score↑	Force MSE↓
NCF [7]	0.043	N/A
No-Tactile	0.539	0.0146
Ablation - 2D Tactile Enc.	0.531	0.0147
Ablation - BCE Loss	0.123	0.0146
Ours (Sim-Only)	0.587	0.0147

TABLE II: Real-World Evaluation: Alignment & Generalization

Model	Scrapers (Seen Class)		Crayons (Unseen in Real)	
	F1 Score↑	Force MSE↓	F1 Score↑	Force MSE↓
Sim-Only	0.002	0.0435	0.008	0.0284
Real-Only	0.458	0.0221	0.614	0.0106
No-Tactile	0.411	0.0432	0.552	0.0115
Ours (Aligned)	0.534	0.0254	0.657	0.0085



Fig. 4: **Left:** Real robot experiment setup: We use a Franka Emika Panda robot with 2 Gelsight Mini tactile sensors mounted on the gripper fingers, and 3 RealSense D435 cameras to capture RGBD observations. **Right:** Training and Testing Tools

1) *Metric 1: Architecture Validation (Sim-to-Sim):* We first verify the architecture’s capacity to learn complex contact physics using a held-out test set from our simulation dataset. This controlled setting allows us to compare architectural choices without domain shift noise. We report the **F1 Score** for binary contact detection and the **Mean Squared Error (MSE)** for force vector regression.

As shown in Table I, our **Tactile-as-PointCloud** architecture trained with Focal Loss outperforms the CNN-based and the BCE Loss variants, confirming effect of preserving the 3D spatial structure of tactile markers and the importance of Focal Loss in estimating extrinsic contact with imbalanced distribution. NCF performs poorly likely due to its sensitivity to varying tool poses, which our method handles natively. It is noted that most methods have similar Force MSE results, likely due to the low tactile and contact fidelity in simulation.

2) *Metric 2: Real-World Alignment Accuracy:* We assess the efficacy of our pipeline on real-world data. We evaluate on a held-out set of **Scrapers** (Seen in Alignment) and a set of **Crayons** (Unseen in Alignment, but Seen in Sim). Ground truth is generated via our heuristic labeling pipeline.

Table II highlights the severity of the sim-to-real gap; the **Sim-Only** model fails almost completely ($F1 \approx 0.0$). The **Real-Only** model achieves good force estimation performance on seen scrapers, but shows poorer generalization to unseen tools. The **No-Tactile** baseline shows moderate geometric contact detection but fails to capture the actual contact force dynamics. In contrast, **Ours (Aligned)** transfers the sensor alignment learned on scrapers to the Crayon dataset, achieving high accuracy ($F1 0.657$). This demonstrates that aligning the sensor model on a simple tool (scraper) allows the physical

priors learned in simulation to transfer effectively to other tool geometries.

3) *Metric 3: Qualitative Generalization:* Finally, we qualitatively evaluate generalization to the **Peeler** task, where complex interactions with irregular carrots make heuristic ground-truth labeling impossible. For this task, we use a model pre-trained on simulated peeler data but fine-tuned using **only** the real-world scraper dataset. As visualized in Figure 5, the Sim-Only model exhibits significant noise. Our Aligned model, however, produces clean, localized contact fields strictly at the blade-carrot interface, validating that our scraper-based alignment strategy successfully generalizes to complex, curved tools like peelers.

B. Policy Evaluation

Experimental Setup. We evaluate policy performance on a real-world Franka Emika Panda robot. The robot is equipped with a parallel gripper modified to house two GelSight Mini tactile sensors. Visual observations are captured via three calibrated RealSense D435 cameras (front, left, right). We evaluate the Diffusion Policy conditioned on SCFields across three contact-rich tasks (Figure 6).

1) *Baselines and Ablations:* We compare SCFields against the **Vision-Only** baseline based on GenDP [29], and a **Raw Tactile (End-to-End)** baseline, which concatenates raw tactile data directly into the policy observation without explicit physics supervision. Additionally, we evaluate the **Sim-Only Contact Field** and **Real-Only Contact Field** baselines defined in Section IV-A. Finally, a **No Contact Force** ablation isolates explicit contact force vectors by training the policy using only contact probability.

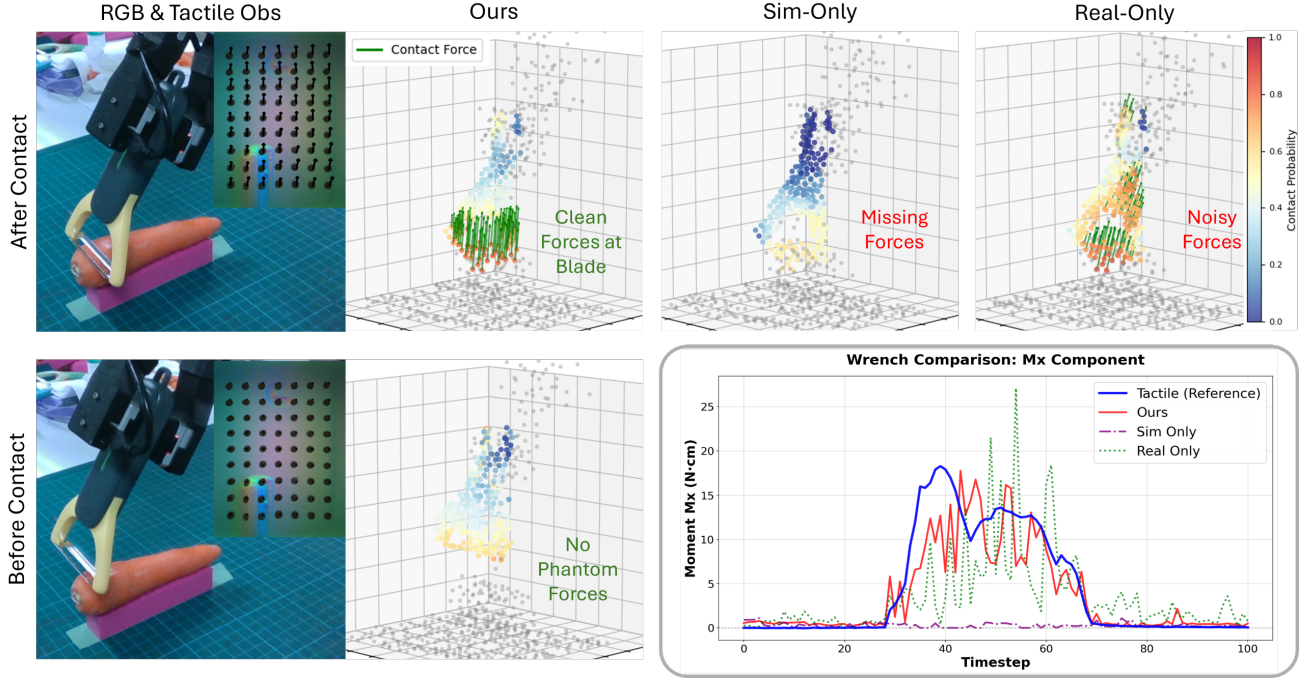


Fig. 5: Qualitative comparison of Contact Field estimation on the Peeler. Left: Ours (clean contact forces on blade), Middle: Sim-Only Model (missing forces). Right: Real-Only Model (noisy forces). **Bottom Right:** Signal Correlation Plot: Torque from Predicted Contact Force (Ours, Sim-Only, Real-Only) vs. Reference Wrench from Tactile Signal. Ours best align with the reference tactile wrench while Real-Only is noisy even when there is no contact

TABLE III: Task 1: Scraper Performance. Ours outperforms baselines on unseen tools, demonstrating robust generalization.

Method	Seen Tools			Unseen Tools		
	SR (%)	Eff (%)	Eff Norm (%)	SR (%)	Eff (%)	Eff Norm (%)
Vision-Only (GenDP)	39.1	10.1	30.5	35.1	25.4	35.1
Raw Tactile	35.1	26.9	35.7	50.0	23.3	27.3
Ours (SCFields)	73.5	61.8	85.2	79.6	73.5	84.7
Ablation: Sim-Only CF	34.5	20.6	33.1	55.6	37.0	45.2
Ablation: Real-Only CF	45.8	32.3	44.5	50.0	47.5	54.2
Ablation: No Force	31.3	22.2	29.9	26.0	24.3	27.6

TABLE IV: Task 2: Crayon Drawing Consistency (Score 0-1).

Method	Seen Crayons	Unseen Crayons
Vision-Only (GenDP)	0.81	0.60
Raw Tactile	0.76	0.61
Ours (SCField)	0.86	0.78
Ablation: Sim-Only CF	0.81	0.60
Ablation: Real-Only CF	0.68	0.74
Ablation: No Force	0.80	0.76

2) Tasks and Metrics: Task 1: Scraper (Contact-Rich

Cleaning. The robot must maintain surface contact to clean debris. We trained the policy on 150 demonstration episodes collected across 3 table heights using 4 training tools. We evaluate on both seen and 4 unseen tools with 2 unseen table heights. Metrics include *Success Rate (SR)* (% of trials maintaining contact) and *Cleaning Efficiency (Eff)* (% of debris removed). An additional *Normalized Efficiency (Eff Norm)* is included to offset the effect of different scraper blade lengths.

Task 2: Crayon Drawing. Picking up an asymmetric crayon

(or pencil) to draw a cross. The policy was trained on 120 episodes across 3 heights using 3 training crayons and was evaluated on 2 unseen heights. Success requires precise force modulation to leave a visible trace without snapping the crayon. Metric: *Drawing Consistency* (0-1 score reflecting completeness/visibility). The preliminary stage of picking up the crayon, which requires visual semantics generalization to unseen crayons/pencils, is reported in Appendix D.

Task 3: Peeler. Peeling a carrot with a handheld peeler. We trained the policy on 60 demonstration episodes using 2 training peelers. This task tests the cross-category generalization of our contact field model as the contact field model was aligned using only scraper data. Metrics: Percentage of Successful Contact and Cut-in, and Peel Quality (avg. peel length).

3) Analysis: We present the quantitative results for all three tasks in Tables III, IV, and V.

Comparison with Baselines. Across all tasks (Tables III, IV, V), SCFields significantly outperforms baselines, particularly on unseen tools. The *Raw Tactile* baseline struggles (e.g.,

TABLE V: Task 3: Peeler Results. Aligned model performance validates the pipeline.

Method	Seen Peelers			Unseen Peelers		
	Contact (%)	Cut-in (%)	Avg Peel Length (cm)	Contact (%)	Cut-in (%)	Avg Peel Length (cm)
Vision-Only	45.0	30.0	1.50	50.0	33.3	1.12
Raw Tactile	45.0	20.0	1.05	40.0	30.0	0.85
Ours (SCField)	80.0	70.0	4.73	90.0	73.3	4.52
Ablation: Sim-Only CF	60.0	30.0	2.00	50.0	46.7	3.05
Ablation: Real-Only CF	60.0	15.0	0.93	57.5	50.0	1.80
Ablation: No Force	65.0	30.0	1.95	40.0	13.3	1.08

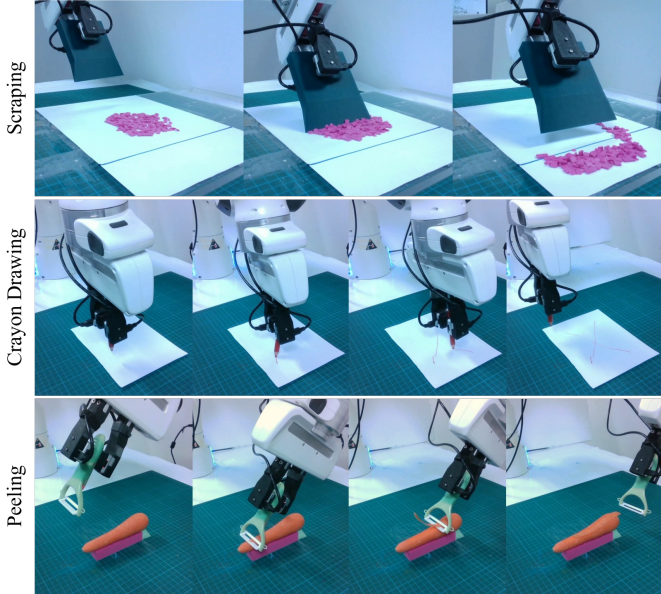


Fig. 6: Rollouts of contact-rich tasks with unseen tools. **Top:** Scraping debris past a target line. **Middle:** Drawing a cross with consistent force. **Bottom:** Peeling a carrot. Additional experiment visualizations are available in Appendix E.

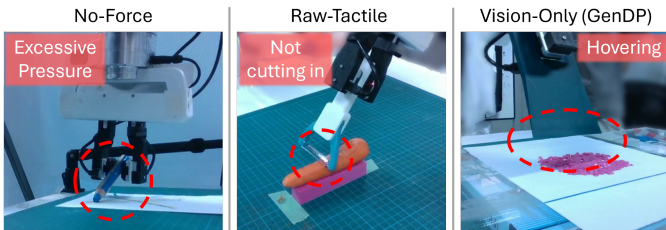


Fig. 7: Example failure modes of baseline/ablation methods.

23.3% Eff on Unseen Scraper), confirming that without explicit physical grounding, end-to-end policies fail to leverage high-dimensional tactile data effectively, often overfitting to visual inputs. Similarly, the *Sim-Only CF* baseline generally matches Vision-Only performance, underscoring that without our real-world alignment stage, the domain gap renders tactile predictions unreliable. Conversely, while the *Real-Only CF* ablation achieves better performance than other baselines on the seen scraper task, it fails to generalize to novel tools, confirming that simulation pre-training is requisite for learning contact representations that transfer across object categories.

Role of Explicit Force & Generalization. The **No Force**

ablation provides critical insight: while it achieves moderate contact detection, the policy exhibits ineffective behaviors like hovering (due to proximity ambiguity) or excessive pressure (slipping crayons). This leads to poor performance on fine-manipulation tasks, demonstrating that contact probability alone is insufficient; explicit force vectors are essential for regulating interaction dynamics. Similar failure modes are also present in other baseline methods that do not explicitly model contact force, as illustrated in figure 7. Notably, the Peeler task highlights the robustness of our pipeline: although the policy used imitation learning on peeling demonstrations, the underlying perception model was aligned using only scraper data. Despite this, our model achieves an average peel length of **4.52cm**, quadrupling the Vision-Only baseline (**1.12cm**). This confirms that SCFields successfully transfers the invariant concept of "functional contact" from simulation to novel real-world tools.

V. CONCLUSION

In this work, we presented **Semantic-Contact Fields (SCFields)**, a novel 3D representation that fuses visual semantics with dense, physically-grounded contact estimates to enable category-level generalization of contact-rich tool manipulation. We addressed the fundamental challenge of tactile sim-to-real transfer through a two-stage learning pipeline: pre-training on large-scale physics simulations to learn geometric contact priors, followed by a data-efficient real-world alignment stage. This approach effectively bridges the reality gap without expensive instrumentation or high-fidelity simulation. Experiments on scraping, drawing, and peeling demonstrate that SCFields significantly outperforms baselines; by grounding sparse tactile readings into dense physical estimates, our system achieves zero-shot generalization to novel tool variants and robustness to dynamic environments where traditional methods fail.

A key limitation of the current framework is its reliance on imitation learning, which restricts the robot to tool usage patterns present in the demonstrations. While SCFields enable robust generalization across geometric variants within a category, the system cannot currently discover novel functional affordances or alternative ways of using tools—such as re-purposing a knife to peel a carrot. Exploring Reinforcement Learning or World Models to enable the autonomous discovery of such creative tool manipulation strategies would be a valuable future direction.

REFERENCES

[1] Iretiayo Akinola, Jie Xu, Jan Carius, Dieter Fox, and Yashraj Narang. Tacsl: A library for visuotactile sensor simulation and learning. *IEEE Transactions on Robotics*, 2025.

[2] Jianxin Bi, Kevin Yuchen Ma, Ce Hao, Mike Zheng Shou, and Harold Soh. Vla-touch: Enhancing vision-language-action models with dual-level tactile feedback. *arXiv preprint arXiv:2507.17294*, 2025.

[3] Zihan Ding, Ya-Yen Tsai, Wang Wei Lee, and Bidan Huang. Sim-to-real transfer for robotic manipulation with tactile sensory. In *2021 IEEE/RSJ International Conference on Intelligent Robots and Systems (IROS)*, pages 6778–6785. IEEE, 2021.

[4] A. Domahidi, E. Chu, and S. Boyd. ECOS: An SOCP solver for embedded systems. In *European Control Conference (ECC)*, pages 3071–3076, 2013.

[5] Theophile Gervet, Zhou Xian, Nikolaos Gkanatsios, and Katerina Fragkiadaki. Act3d: 3d feature field transformers for multi-task robotic manipulation. In *Conference on Robot Learning*, pages 3949–3965. PMLR, 2023.

[6] Zihao He, Hongjie Fang, Jingjing Chen, Hao-Shu Fang, and Cewu Lu. FoAR: Force-aware reactive policy for contact-rich robotic manipulation. *IEEE Robotics and Automation Letters*, 10(6):5625–5632, 2025. doi: 10.1109/LRA.2025.3560871.

[7] Carolina Higuera, Siyuan Dong, Byron Boots, and Mustafa Mukadam. Neural contact fields: Tracking extrinsic contact with tactile sensing. In *2023 IEEE International Conference on Robotics and Automation (ICRA)*, pages 12576–12582. IEEE, 2023.

[8] Carolina Higuera, Joseph Ortiz, Haozhi Qi, Luis Pineda, Byron Boots, and Mustafa Mukadam. Perceiving extrinsic contacts from touch improves learning insertion policies. *arXiv preprint arXiv:2309.16652*, 2023.

[9] Carolina Higuera, Akash Sharma, Chaithanya Krishna Bodduluri, Taosha Fan, Patrick Lancaster, Mrinal Kalakrishnan, Michael Kaess, Byron Boots, Mike Lambeta, Tingfan Wu, and Mustafa Mukadam. Sparsh: Self-supervised touch representations for vision-based tactile sensing. In *8th Annual Conference on Robot Learning*, 2024. URL <https://openreview.net/forum?id=xYJn2e1uu8>.

[10] Binghao Huang, Yixuan Wang, Xinyi Yang, Yiyue Luo, and Yunzhu Li. 3d-vitac: Learning fine-grained manipulation with visuo-tactile sensing. In *8th Annual Conference on Robot Learning*, 2024. URL <https://openreview.net/forum?id=bk28W1kqZn>.

[11] Tsung-Wei Ke, Nikolaos Gkanatsios, and Katerina Fragkiadaki. 3d diffuser actor: Policy diffusion with 3d scene representations. In *8th Annual Conference on Robot Learning*.

[12] Leon Kim, Yunshuang Li, Michael Posa, and Dinesh Jayaraman. Im2contact: Vision-based contact localization without touch or force sensing. In *Conference on Robot Learning*, pages 1533–1546. PMLR, 2023.

[13] Jayjun Lee and Nima Fazeli. Vitascope: Visuo-tactile implicit representation for in-hand pose and extrinsic contact estimation. In *Robotics: Science and Systems (RSS)*, 2025.

[14] Tsung-Yi Lin, Priya Goyal, Ross Girshick, Kaiming He, and Piotr Dollár. Focal loss for dense object detection. In *Proceedings of the IEEE international conference on computer vision*, pages 2980–2988, 2017.

[15] Yijiong Lin, Alex Church, Max Yang, Haoran Li, John Lloyd, Dandan Zhang, and Nathan F Lepora. Bi-touch: Bimanual tactile manipulation with sim-to-real deep reinforcement learning. *IEEE Robotics and Automation Letters*, 8(9):5472–5479, 2023.

[16] Fangchen Liu, Kuan Fang, Pieter Abbeel, and Sergey Levine. Moka: Open-world robotic manipulation through mark-based visual prompting. *arXiv preprint arXiv:2403.03174*, 2024.

[17] Jason Jingzhou Liu, Yulong Li, Kenneth Shaw, Tony Tao, Ruslan Salakhutdinov, and Deepak Pathak. Factr: Force-attending curriculum training for contact-rich policy learning. *arXiv preprint arXiv:2502.17432*, 2025.

[18] Wenhui Liu, Junbo Wang, Yiming Wang, Weiming Wang, and Cewu Lu. Forceimic: Force-centric imitation learning with force-motion capture system for contact-rich manipulation. In *2025 IEEE International Conference on Robotics and Automation (ICRA)*, pages 1105–1112. IEEE, 2025.

[19] Daolin Ma, Siyuan Dong, and Alberto Rodriguez. Extrinsic contact sensing with relative-motion tracking from distributed tactile measurements. In *2021 IEEE international conference on robotics and automation (ICRA)*, pages 11262–11268. IEEE, 2021.

[20] Viktor Makoviychuk, Lukasz Wawrzyniak, Yunrong Guo, Michelle Lu, Kier Storey, Miles Macklin, David Hoeller, Nikita Rudin, Arthur Allshire, Ankur Handa, et al. Isaac gym: High performance gpu-based physics simulation for robot learning. *arXiv preprint arXiv:2108.10470*, 2021.

[21] Charles Ruizhongtai Qi, Li Yi, Hao Su, and Leonidas J Guibas. Pointnet++: Deep hierarchical feature learning on point sets in a metric space. *Advances in neural information processing systems*, 30, 2017.

[22] Daniel Seita, Yufei Wang, Sarthak J Shetty, Edward Yao Li, Zackory Erickson, and David Held. Toolflownet: Robotic manipulation with tools via predicting tool flow from point clouds. In *Conference on Robot Learning*, pages 1038–1049. PMLR, 2023.

[23] Zilin Si and Wenzhen Yuan. Taxim: An example-based simulation model for gelsight tactile sensors. *IEEE Robotics and Automation Letters*, 7(2):2361–2368, 2022.

[24] Anukriti Singh, Kasra Torshizi, Khuzema Habib, Kelin Yu, Ruohan Gao, and Pratap Tokekar. Afford2act: Affordance-guided automatic keypoint selection for generalizable and lightweight robotic manipulation. *arXiv preprint arXiv:2510.01433*, 2025.

- [25] Chao Tang, Anxing Xiao, Yuhong Deng, Tianrun Hu, Wenlong Dong, Hanbo Zhang, David Hsu, and Hong Zhang. Functo: Function-centric one-shot imitation learning for tool manipulation. *arXiv preprint arXiv:2502.11744*, 2025.
- [26] Chao Tang, Anxing Xiao, Yuhong Deng, Tianrun Hu, Wenlong Dong, Hanbo Zhang, David Hsu, and Hong Zhang. Mimicfunc: Imitating tool manipulation from a single human video via functional correspondence. In *Conference on Robot Learning*, pages 4473–4492. PMLR, 2025.
- [27] Shaoxiong Wang, Mike Lambeta, Po-Wei Chou, and Roberto Calandra. Tacto: A fast, flexible, and open-source simulator for high-resolution vision-based tactile sensors. *IEEE Robotics and Automation Letters*, 7(2):3930–3937, 2022.
- [28] Yixuan Wang, Mingtong Zhang, Zhuoran Li, Katherine Rose Driggs-Campbell, Jiajun Wu, Li Fei-Fei, and Yunzhu Li. D³ fields: Dynamic 3d descriptor fields for zero-shot generalizable robotic manipulation. In *ICRA 2024 Workshop on 3D Visual Representations for Robot Manipulation*, 2023.
- [29] Yixuan Wang, Guang Yin, Binghao Huang, Tarik Kestemur, Jiuguang Wang, and Yunzhu Li. Gendp: 3d semantic fields for category-level generalizable diffusion policy. In *8th Annual Conference on Robot Learning*, volume 2, 2024.
- [30] Yunlong Wang, Lei Zhang, Yuyang Tu, Hui Zhang, Kaixin Bai, Zhaopeng Chen, and Jianwei Zhang. Tooleenet: Tool affordance 6d pose estimation. In *2024 IEEE/RSJ International Conference on Intelligent Robots and Systems (IROS)*, pages 10519–10526. IEEE, 2024.
- [31] Wenzhen Yuan, Siyuan Dong, and Edward H Adelson. Gelsight: High-resolution robot tactile sensors for estimating geometry and force. *Sensors*, 17(12):2762, 2017.
- [32] Yanjie Ze, Gu Zhang, Kangning Zhang, Chenyuan Hu, Muhan Wang, and Huazhe Xu. 3d diffusion policy: Generalizable visuomotor policy learning via simple 3d representations. *arXiv preprint arXiv:2403.03954*, 2024.
- [33] Jialiang Zhao, Yuxiang Ma, Lirui Wang, and Edward Adelson. Transferable tactile transformers for representation learning across diverse sensors and tasks. In *8th Annual Conference on Robot Learning*, 2024. URL <https://openreview.net/forum?id=KXsropnmNI>.
- [34] Haoyu Zhen, Xiaowen Qiu, Peihao Chen, Jincheng Yang, Xin Yan, Yilun Du, Yining Hong, and Chuang Gan. 3d-vla: A 3d vision-language-action generative world model. In *International Conference on Machine Learning*, pages 61229–61245. PMLR, 2024.

APPENDIX

A. Network Architecture Details

We utilize a PointNet++ [21] architecture to process the heterogeneous input point cloud. The network consists of a series of Set Abstraction (SA) layers for feature downsampling and Feature Propagation (FP) layers for upsampling.

Input: The input is a point cloud of size $(N, 3 + C_{in})$, where $N = 894$ (256 object + 512 environment + 126 tactile) and $C_{in} = 16$ (1 type channel + 15 tactile history channels).

Encoder (Set Abstraction):

- **SA1:** Number of points: 512, Radius: 0.02m, Samples: 32, MLP: [32, 32, 64].
- **SA2:** Number of points: 128, Radius: 0.04m, Samples: 64, MLP: [64, 64, 128].
- **SA3 (Global):** Number of points: None (Global pooling), MLP: [128, 128, 256].

Decoder (Feature Propagation):

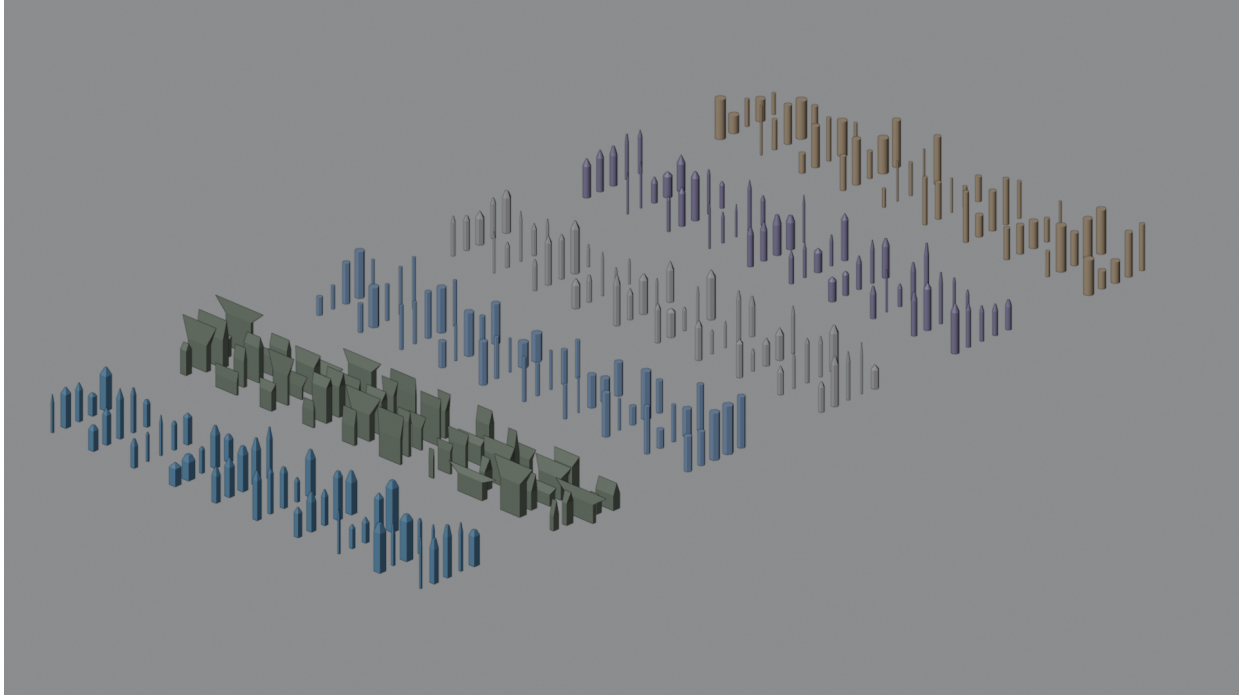
- **FP1:** Interpolates features from SA3 to SA2. MLP: [256, 256].
- **FP2:** Interpolates features from FP1 to SA1. MLP: [256, 128].
- **FP3:** Interpolates features from FP2 to the original input points. MLP: [128, 128, 128].

Prediction Heads: The decoded features (dim 128) are passed to two parallel heads:

- 1) **Contact Probability Head:** MLP: [64, 32, 1] followed by a Sigmoid activation.
- 2) **Force Regression Head:** MLP: [64, 32, 3] (No activation).

B. Simulation and Data Labeling Details

As described in Section III-B2, we employ a two-stage replay process to generate dense ground-truth labels from rigid-body simulation data. This section details the simulation configuration and the mathematical formulation used to map discrete rigid-body states to dense contact fields.



1) *Simulation Environments and Tactile Modeling:* Our simulation pipeline utilizes the TacSL framework [1] to model the physics of the GelSight sensor within IsaacGym [20]. We define a uniform 7×9 marker grid that matches the physical distribution of the GelSight Mini sensors used in our real-world experiments.

We employ TacSL's penalty-based tactile model to derive shear force distributions and surface depth maps at each marker location. This point-based representation serves as a transferable input for our architecture, maintaining consistency across both simulated and real tactile data streams.

Simulation Configuration We provide the specific physical and control parameters used in our IsaacGym and TacSL setup in Listing 1. The compliance parameters were randomized during training to improve the robustness of the learned policies.

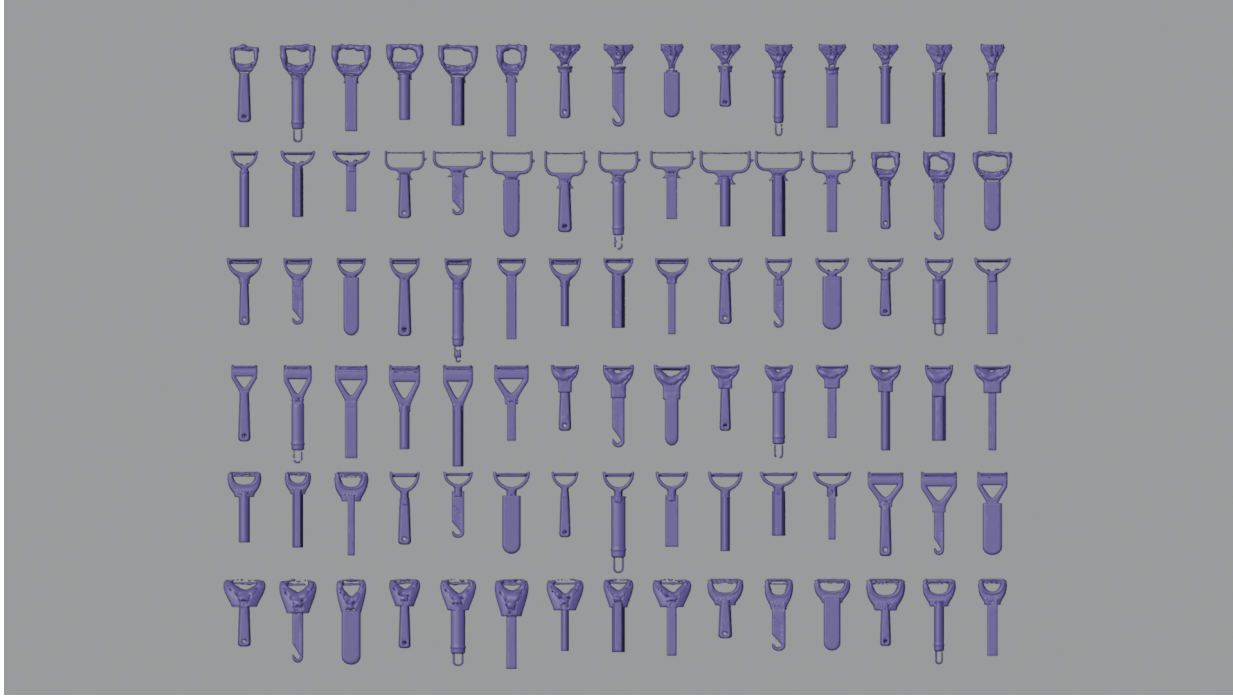


Fig. 8: Peeler meshes used in simulation

Listing 1: Key Simulation and TacSL parameters.

```

TacSL:
  compliance_stiffness_range: [1400, 1500]
  compliant_damping_range: [1.5, 2.5]
  elastomer_friction: 5.0

IsaacGym:
  substeps: 4
  physx:
    num_pos_iterations: 32
    num_vel_iterations: 2
    contact_offset: 0.002
    max_depenetration_vel: 1.0
    friction_corr_dist: 0.001

Robot_Control:
  gripper_prop_gains: [800, 800]
  gripper_deriv_gains: [4, 4]
  task_space_impedance: # cartesian
    prop_gains: [800, 800, 600, 100, 100, 100]
    deriv_gains: [100, 100, 75, 3, 3, 3]
    # prop_gains randomization range
    kp_min: [300, 300, 300, 20, 20, 20]
    kp_max: [800, 800, 800, 60, 60, 60]

```

Listing 2: Tactile filtering and smoothing parameters.

```

Tactile_Filtering:
  spatial:
    enabled: true
    method: "gaussian"
    sigma: 0.25
  temporal:
    enabled: true
    window_length: 7
    polyorder: 1

Contact_Smoothing:
  precontact_smoothing: true
  postcontact_smoothing: true
  method: "linear"
  depth_threshold: -0.002

```

2) *Tactile Data Post-Processing*: To improve the quality of the tactile signal, we apply a multi-stage post-processing pipeline to the raw simulated tactile data. This includes spatial filtering to emulate the elastic diffusion of the elastomer, temporal filtering to reduce simulation jitter, and contact-phase smoothing to ensure a clean baseline.

Spatial and Temporal Filtering We apply a spatial Gaussian filter to the 7×9 marker grid to simulate the physical coupling between adjacent taxels in a real elastomer. Additionally, a temporal Savitzky-Golay filter is applied across a sliding window of timesteps to suppress high-frequency noise inherent in the physics solver's penalty-based contact model.

Contact-Phase Smoothing A significant challenge in simulated tactile data is the presence of non-zero force residuals when the sensor is not in contact. To address this, we implement a phase-aware smoothing strategy. Based on the ground-truth contact depth, we identify the *pre-contact* (approach) and *post-contact* (lifting) phases. As detailed in Listing 2, we apply a

linear interpolation from the phase median to the boundary contact value, effectively neutralizing sensor drift and simulation artifacts during non-contact states.

We observe that tactile simulation fidelity is highly sensitive to physical parameters. Despite rigorous tuning and data filtering, the quality of simulated tactile signals remains limited, as detailed in Section IV-A. This persistent discrepancy underscores the critical necessity of our real-world alignment stage to effectively bridge the sim-to-real gap.

3) *Soft Contact Probability Labeling*: Rigid-body simulators typically treat contact as a binary and unstable state. To generate smooth, learnable contact probability labels, we utilize the Signed Distance Function (SDF) computed in Open3D. We map the penetration depth d_i (where $d_i < 0$ indicates penetration) of each point p_i on the tool surface to a continuous contact probability $c_i \in [0, 1]$ using a one-sided exponential decay function:

$$c_i = P(contact|d_i) = \exp\left(-\left(\frac{\max(-d_i, 0)}{\lambda}\right)^k\right) \quad (3)$$

where $k = 1.7$ controls the sharpness of the boundary, providing a smooth, Gaussian-like falloff. The length-scale parameter λ is computed automatically such that the probability decays to 0.5 at a penetration depth of 5mm. This formulation ensures that points deep inside the object (indicating strong contact) have probabilities near 1.0, while points merely grazing the surface are assigned intermediate values.

4) *Dense Force Labeling by Extrapolation*: PyBullet provides discrete contact manifolds consisting of a sparse set of contact positions $\{\mathbf{x}_j\}$, normal vectors $\{\mathbf{n}_j\}$, and force magnitudes $\{F_j\}$. To transform these sparse interactions into a dense force field \mathbf{f}_i^{ext} defined over the tool’s point cloud, we employ a distance-weighted kernel interpolation modulated by local geometry.

For every point p_i on the tool mesh, the extrapolated force vector is computed as:

$$\mathbf{f}_i^{ext} = S(d_i) \cdot \frac{\sum_j w_{ij} (F_j \mathbf{n}_j)}{\sum_j w_{ij}} \quad (4)$$

Distance Weighting (w_{ij}): We determine the influence of a discrete contact j on mesh point i using an inverse-square kernel based on their Euclidean distance:

$$w_{ij} = \frac{1}{1 + (\lambda_{dist} \|\mathbf{x}_j - p_i\|)^2} \quad (5)$$

where $\lambda_{dist} = 50.0$ controls the locality, ensuring forces are concentrated around the active contact region.

Depth Modulation: To obtain smoother force distribution and prevent non-contacting points accumulate large amount of forces due to kernel interpolation, we scale the extrapolated force by the point’s local penetration depth:

$$S(d_i) = \sqrt{\text{ReLU}\left(1 - \frac{d_i}{d_{thresh}}\right)} \quad (6)$$

where $d_{thresh} = -5\text{mm}$. This term ensures that the force magnitude tapers smoothly to zero as a point moves away from the penetration surface. Finally, we apply spatial outlier clipping (98th percentile) to remove numerical spikes inherent to rigid-body collision solving.

5) *Real-World Sensor Calibration*: To bridge the gap between simulated and real tactile readings, we perform a force calibration procedure on the real GelSight sensors. The calibration involves making the gripper grasp a reference block and then applying a known external force by placing a calibrated weight on the block. During this interaction, we monitor the change in the total wrench, which is computed from the tactile marker displacement and the depth map.

We calculate a scaling factor to align the magnitude of the computed tactile wrench with the known applied external wrench. It is important to note that this process does not aim to establish a precise, non-linear mapping from tactile signals to contact forces. Instead, it serves as a linear alignment step to ensure that the scale of the tactile signals in the real world matches the dynamic range observed in simulation, facilitating robust sim-to-real transfer.

C. Training Hyperparameters and Loss Functions

1) *Contact Field Loss Functions*: We optimize the network using a composite loss function:

$$\mathcal{L}_{total} = \lambda_{prob}\mathcal{L}_{prob} + \lambda_{force}(\lambda_{mag}\mathcal{L}_{mag} + \lambda_{dir}\mathcal{L}_{dir}) \quad (7)$$

where $\lambda_{prob} = 1.0$ and $\lambda_{force} = 2.0$. Within the force term, the components are weighted by $\lambda_{mag} = 1.5$ and $\lambda_{dir} = 1.0$.

Contact Probability Loss (\mathcal{L}_{prob}): We use the Focal Loss to handle the extreme class imbalance (contact vs. free space):

$$\mathcal{L}_{prob} = -\alpha_t (1 - p_t)^\gamma \log(p_t) \quad (8)$$

where p_t is the model’s estimated probability for the true class, with focusing parameter $\gamma = 0.75$ and balancing factor $\alpha = 0.9$ for the positive class.

Force Magnitude Loss (\mathcal{L}_{mag}): We use a Mean Squared Error (MSE) loss on the force norms, with adaptive weighting to prioritize high-force regions:

$$\mathcal{L}_{mag} = w_i (\|\mathbf{f}^{pred}\| - \|\mathbf{f}^{gt}\|)^2 \quad (9)$$

where w_i is a log-magnitude adaptive weight $w_i \propto \log(1 + \|\mathbf{f}^{gt}\|)$ clipped to $[1.0, 3.0]$.

Force Direction Loss (\mathcal{L}_{dir}): We use Cosine Similarity loss, applied only to points where the ground truth force magnitude exceeds a threshold $\tau = 0.005N$:

$$\mathcal{L}_{dir} = 1 - \frac{\mathbf{f}^{pred} \cdot \mathbf{f}^{gt}}{\max(\|\mathbf{f}^{pred}\| \|\mathbf{f}^{gt}\|, \epsilon)} \quad (10)$$

2) *Contact Field Training Schedule:* Table VI summarizes the training parameters.

TABLE VI: Contact Field Model Training Hyperparameters

Parameter	Stage 1 (Sim)	Stage 2 (Real)
Optimizer	AdamW	AdamW
Learning Rate	$1e^{-4}$	$5e^{-6}$
LR Scheduler	ReduceLROnPlateau	ReduceLROnPlateau
Batch Size	320	128
Epochs	400	60
Point Translation	$\pm 0.1m$	$\pm 0.05m$
Point Rotation	$\pm 30^\circ$ (Z-axis)	$\pm 15^\circ$ (Z-axis)
Jitter Noise (σ)	0.01	0.01
Tactile Noise (σ)	0.001	0.001

3) *Diffusion Policy Hyperparameters:* We utilize a Diffusion Policy modeled as a conditional U-Net to predict robot actions. The policy takes a history of $T_{obs} = 3$ observations and predicts a sequence of action steps with a prediction horizon of $T = 16$, executing $T_{action} = 8$ steps before replanning. The specific hyperparameters are detailed in Table VII.

TABLE VII: Diffusion Policy Hyperparameters

Parameter	Value
<i>Policy Configuration</i>	
Observation Horizon (T_{obs})	3
Action Execution (T_{action})	8
Prediction Horizon (T)	16
Action Type	Delta End-Effector Pose
<i>Optimization</i>	
Optimizer	AdamW
Learning Rate	$1e^{-4}$
Weight Decay	$1e^{-6}$
LR Scheduler	Cosine w/ 500 warmup steps
Batch Size	128
Epochs	1000
EMA	Enabled (Power 0.75)

D. Crayon Picking Experiment

Although not the primary focus of this work, we conducted a crayon picking experiment to evaluate the utility of the semantic field as a prerequisite capability for the drawing task. The experiment entails identifying and grasping a crayon or pencil placed on a holder, as illustrated in Figure 9.

Given the asymmetric geometry of the tools, the robot must explicitly grasp the handle rather than the writing tip to enable subsequent use. We evaluate our method against a baseline that excludes the semantic field, relying solely on the contact field, point cloud coordinates (XYZ), and *RGB* information. Both models were trained for 60 epochs using the dataset collected from the three training crayons shown in Figure 4.

We assess performance using two metrics: *Directional Accuracy* (the percentage of trials where the robot approaches the correct handle side) and *Grasp Success Rate* (the percentage of successful lifts). As detailed in Table VIII, the inclusion of the semantic field significantly improves performance.

The second column in Figure 9 qualitatively demonstrates that our model infers generalized semantic fields across both seen and unseen crayons/pencils, successfully highlighting the tip area to avoid. The quantitative results further confirm that

TABLE VIII: Crayon Picking Experimental Results. We report the Directional Accuracy (Dir. Acc.) and Grasp Success Rate (Success) on seen and unseen objects.

Method	Seen Objects		Unseen Objects	
	Dir. Acc.	Success	Dir. Acc.	Success
Baseline (w/o Semantic)	63.3%	33.3%	40.0%	23.3%
Ours (w/ Semantic)	93.3%	76.7%	93.3%	73.3%

the semantic field enables the policy to consistently identify the handle location and approach from the correct direction. Conversely, the baseline policy often fails to distinguish the handle from the tip, resulting in performance close to random guessing, particularly on unseen objects.

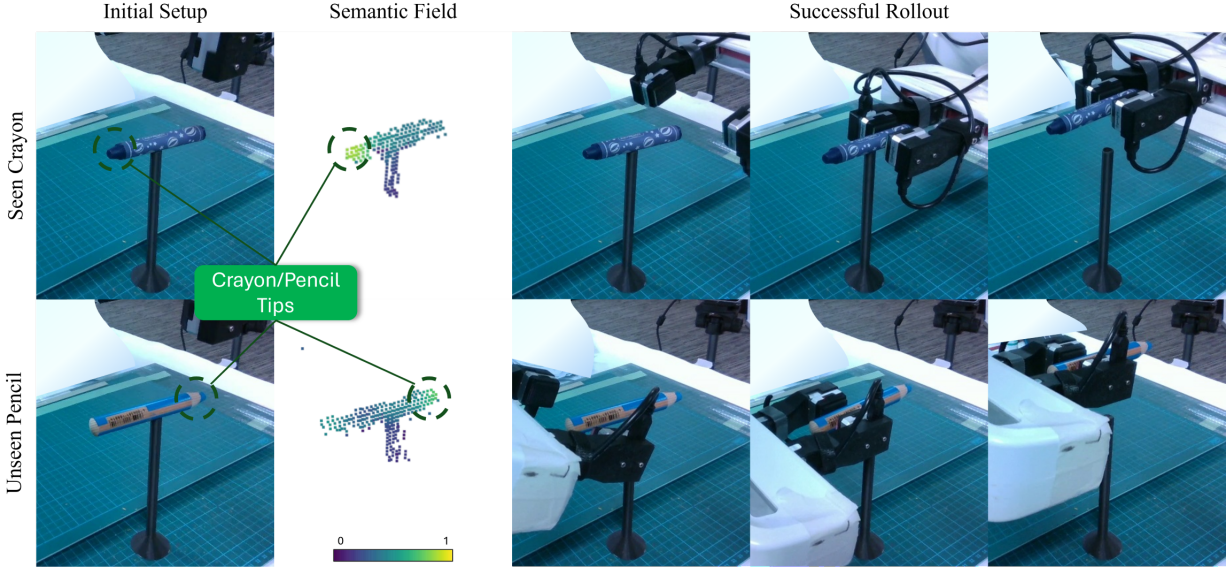


Fig. 9: Illustration of the crayon picking setup, Semantic Field visualization, and successful rollouts on both seen and unseen instances. The Semantic Field is able to distinguish between the tip and handle in both seen and unseen crayons/pencils, guiding the robot to pick up from the correct direction.

E. Additional Experiment Details and Qualitative Analysis

1) *Details on Evaluation Metrics for Scraping Task:* In the scraping task described in the main text, we employ two primary metrics to evaluate performance: Scraping Efficiency (*Eff*) and Normalized Scraping Efficiency (*Eff Norm*).

- **Scraping Efficiency (*Eff*):** This metric measures the percentage of debris successfully removed. We weigh the debris pushed behind the target line (the blue line) using a precision scale. The efficiency is defined as the ratio of cleaned weight to total weight:

$$\text{Eff} = \frac{W_{\text{cleaned}}}{W_{\text{total}}} \quad (11)$$

- **Normalized Scraping Efficiency (*Eff Norm*):** Tools with longer blades naturally cover a larger area and tend to achieve higher raw scraping efficiency. Since the tools in our test set possess a longer average blade length than those in the training set, direct comparison using raw efficiency is biased. To account for this geometric advantage, we normalize the efficiency by the tool's blade length. We define a reference blade length ratio $L_{\text{ref}} = L_{\text{blade}}/L_{\text{max}}$, where L_{max} is the length of the longest blade across all tools. The normalized efficiency is computed as:

$$\text{Eff Norm} = \min \left(1, \frac{\text{Eff}}{L_{\text{ref}}} \right) \quad (12)$$

This metric rewards policies that maximize the utility of the available tool geometry.

2) *Qualitative Evaluation of Contact Field Prediction:* To evaluate the robustness of our contact field estimation, we provide qualitative comparisons between the model's predictions and the ground truth (or pseudo-ground truth) data across both simulated and real-world domains.

a) *Simulation Results*: Figure 10 illustrates the contact field prediction in the simulation environment. The model accurately reconstructs the contact geometry compared to the ground truth provided by the TacSL physics engine.

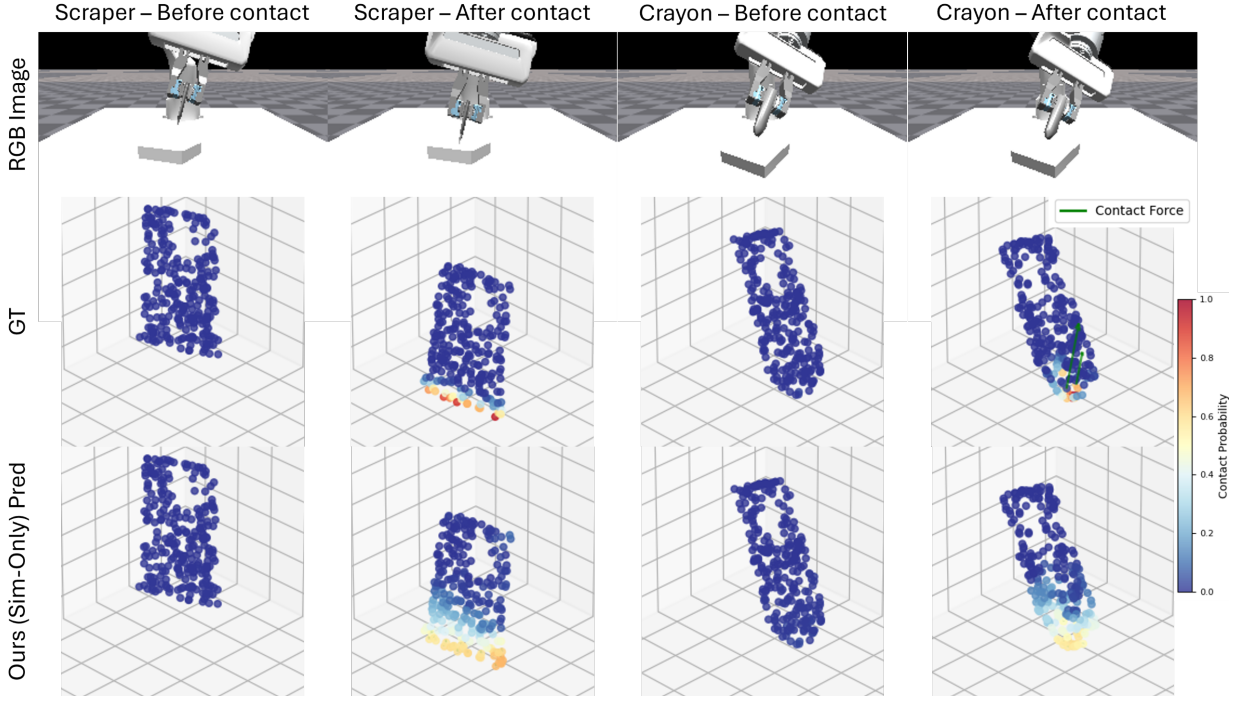


Fig. 10: Qualitative results in simulation. The predicted contact probabilities (bottom row) closely match the ground truth fields (middle row) generated by the simulation pipeline.

b) *Real-World Results*: In the real-world experiments, absolute ground truth for the contact field is unavailable. Instead, we generate a "pseudo-ground truth" derived from high-resolution depth maps captured by the GelSight sensor. Figure 11 displays the predictions for both the scraping tool and the crayon grasping task. Despite the domain shift, the model successfully infers contact patches that align with the physical interaction areas.

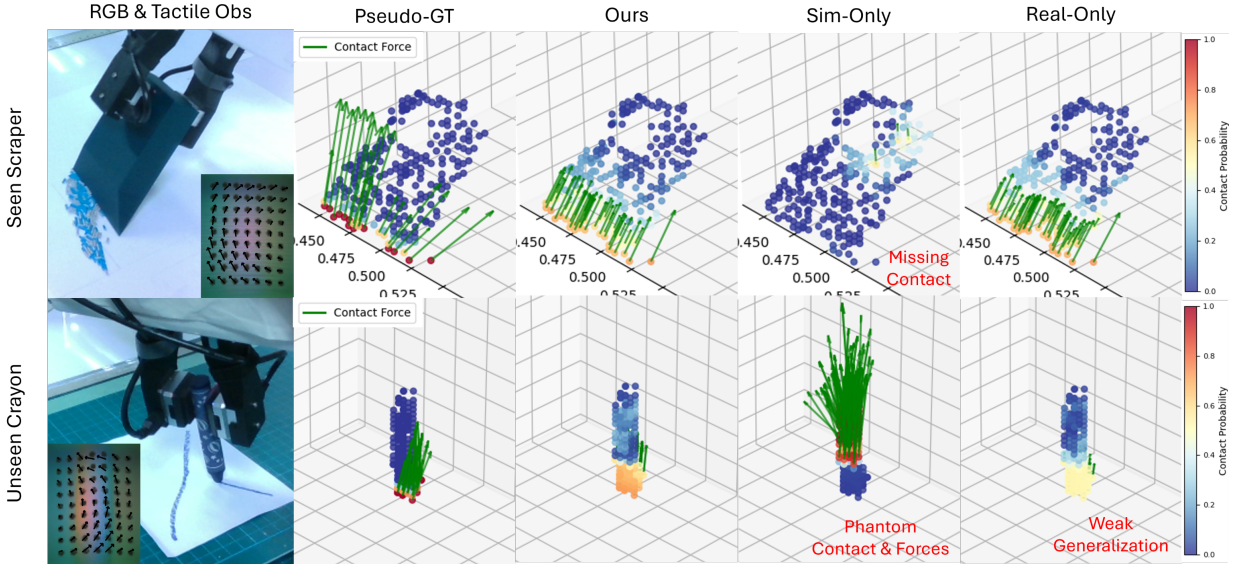


Fig. 11: Qualitative results in the real world. We compare the predicted contact fields by **Ours**, **Sim-Only** baseline, and **Real-Only** baseline against pseudo-ground truth for the scraping tool (top) and the crayon (bottom). The Sim-Only baseline produces missing or phantom contact and forces. The Real-Only model performs well on scraper seen in training data, but is worse than ours in generalizing to the unseen crayon.